Article

Threshold Ranges of Multiphase Components from Natural Ice CT Images Based on Watershed Algorithm

Shengbo Hu [1] , Qingkai Wang [1], Chunjiang Li [2] and Zhijun Li [1,*]

[1] State Key Laboratory of Coastal and Offshore Engineering, Dalian University of Technology, Dalian 116024, China; hushengbo@mail.dlut.edu.cn (S.H.); wangqingkai@dlut.edu.cn (Q.W.)
[2] School of Energy and Environment, Inner Mongolia University of Science and Technology, Baotou 014010, China; lichunjiang0405@imust.edu.cn
* Correspondence: lizhijun@dlut.edu.cn

Abstract: The multiphase components of natural ice contain gas, ice, unfrozen water, sediment and brine. X-ray computed tomography (CT) analysis of ice multiphase components has the advantage of high precision, non-destructiveness and visualization; however, it is limited by the segmentation thresholds. Due to the proximity of the CT value ranges of gas, ice, unfrozen water, sediment and brine within the samples, there is uncertainty in the artificial determination of the CT image segmentation thresholds, as well as unsuitability of the global threshold segmentation methods. In order to improve the accuracy of multi-threshold segmentation in CT images, a CT system was used to scan the Yellow River ice, the Wuliangsuhai lake ice and the Arctic sea ice. The threshold ranges of multiphase components within the ice were determined by watershed algorithm to construct a high-precision three-dimensional ice model. The results indicated that CT combined with watershed algorithm was an efficient and non-destructive method for obtaining microscopic information within ice, which accurately segmented the ice into multiphase components such as gas, ice, unfrozen water, sediment, and brine. The gas CT values of the Yellow River ice, the Wuliangsuhai lake ice and the Arctic sea ice ranged from -1024 Hu~-107 Hu, -1024 Hu~-103 Hu, and -1024 Hu~-160 Hu, respectively. The ice CT values of the Yellow River ice, the Wuliangsuhai lake ice and the Arctic sea ice ranged from -103 Hu~-50 Hu, -100 Hu~-38 Hu, -153 Hu~-51 Hu. The unfrozen water CT values of the Yellow River ice and the Wuliangsuhai lake ice ranged from -8 Hu~18 Hu, -8 Hu~13 Hu. The sediment CT values of the Yellow River ice and the Wuliangsuhai lake ice ranged from 20 Hu~3071 Hu, 20 Hu~3071 Hu, and the brine CT values of the Arctic sea ice ranged from -6 Hu~3071 Hu. The errors between the three-dimensional ice model divided by threshold ranges and measured sediment content were less than 0.003 g/cm^3, which verified the high accuracy of the established microscopic model. It provided a scientific basis for ice engineering, ice remote sensing, and ice disaster prevention.

Keywords: threshold ranges; natural ice; multiphase components; CT images; watershed algorithm

1. Introduction

Ice is a prevalent molecular crystal in nature, which inevitably contains gas, unfrozen water and sediment due to complex natural conditions [1]. The microstructure of ice reflects its internal "skeleton" characteristics. The non-uniform distribution of components within ice alters its internal structure, which directly impacts its physical properties [2]. For instance, the interaction between ice and structures forms the foundation of ice engineering research, while the mechanical properties of ice are determined by its microstructure [3]. The microstructure of ice also leads to variability in the thermal, optical and electrical properties, which further influences subglacial water ecosystems and forms the basis for ice thermodynamics and ice remote sensing research [4]. Information on the ice growth process is stored in the ice microstructure. Analyzing the microstructure can facilitate the

study of ice growth and melting, thereby improving the accuracy of predictions related to ice sheet breakup, ice jamming, and ice damming [5]. Consequently, obtaining information on the ice microstructure is the key to research on ice engineering, ice remote sensing and ice disaster prevention.

The microstructure of ice has its fundamental physical properties, which mainly includes stratification, crystal structure, and impurities. Currently, common instruments for obtaining ice microstructural information are a Federov rotary stage [6], a scanning electron microscope [7], a nuclear magnetic resonance instrument [8], and an X-ray scanning system [9]. Among the various microanalysis tools, X-ray scanning systems are widely used for analyzing the internal microstructures of samples due to the unique advantages of non-destructiveness and visualization [9]. Researchers have conducted numerous studies to characterize the ice pore structure. Michel et al. [10] qualitatively classified the ice structure by in situ observations and examinations of ice crystals. Shokr et al. [11] conducted field experiments in Resolute Bay to characterize the microstructure characteristics of one-year and multi-year ice based on crystal observations. Cole et al. [12] analyzed the main microstructural types of ice and their origins and discussed the microstructural changes that occurred during deformation. Li et al. [13] performed uniaxial compression experiments on 117 columnar-grained sea ice specimens along the direction parallel to ice surface under different test temperatures and strain rates. The results supported the curved-surface relationship between the uniaxial compressive strength and porosity within a wide range of strain rate. Sammonds et al. [14] considered that ice occurred as polycrystalline aggregates in which the bulk behavior was the result of the behavior of the ensemble of individual grains; therefore, it was dependent on the microstructure, that was to say, the whole arrangement of grains, their internal substructure, impurities, and second phases. Hammonds et al. [15] conducted uniaxial compression experiments on polycrystalline ice samples at different strain rates and temperatures. The extent of cracking from each test is characterized via micro-CT imaging and is quantified via a newly proposed variant of the crack density tensor. Salomon et al. [16] analyzed the three-dimensional microstructure of sea ice by means of X-ray computed tomography. Microscopic (brine and air pore sizes, numbers and connectivity) and macroscopic (salinity, density, porosity) properties of young Arctic sea ice were analyzed. The current research mainly focuses on the relationship between microstructural information obtained through CT systems and macroscopic physical properties. Thus, accurately determining the threshold range of ice components is essential for advancing the study of ice mechanics, thermodynamics and optics, which is also crucial for improving the accuracy of ice numerical modeling.

Recently, X-ray computed tomography (CT) has been increasingly applied to micro-scale studies of materials, including non-destructive testing [17], pore structure analysis [18], compositional delineation [19], and numerical simulation based on CT images [20]. This rise in application is attributed to its advantages of non-destructiveness, dynamic imaging, and continuity [21]. However, compared to common rock microstructures, the CT value ranges of ice, gas, unfrozen water, and sediment within ice microstructures are close to each other, complicating threshold segmentation. Additionally, recent research indicates that there is significant uncertainty in the manual determination of CT image segmentation thresholds, which can lead to errors in analysis [22].

The major objectives of the study included (a) the CT value ranges of different components in the Yellow River ice, Wuliangsuhai Lake ice and Arctic sea ice were summarized, by which the pore morphology was explored. Moreover, the study compared the two-dimensional CT image threshold segmentation results with the field observation; (b) based on the reconstructed three-dimensional ice model, the morphology, distribution of intra-ice sediment and intra-ice pore were extracted, and the reasons for the formation of different morphological bubbles in different types of ice were discussed; (c) the three-dimensional model of the Yellow River ice was reconstructed using CT and digital image processing techniques. The feasibility of the watershed algorithm for ice image threshold segmentation was validated through actual measurements of sediment content at different depths. The

study improved the segmentation accuracy of CT images, which provided an essential foundation for accurate extraction of ice microstructure information.

2. Materials and Methods

2.1. Material

The ice samples for CT analysis were collected from the Yellow River ice, Wuliangsuhai lake ice and Arctic sea ice. The Yellow River ice samples were obtained from Baotou to Toketo County. River ice typically contains not only air bubbles but also impurities such as sediment, which is introduced during the flow of river. Seven ice samples were collected in the Yellow River, which were named in order, such as the Yellow River No. 1 ice sample. Wuliangsuhai, situated in Ulatqian Banner, Bayannur City, Inner Mongolia Autonomous Region, experiences a freeze period from November to March each year. During frozen period, water flows slowly, and the microstructure of lake ice is primarily influenced by localized air bubbles [23]. Two ice samples were collected according to ice surface in the Wuliangsuhai, named the Wuliangsuhai No. 1 ice sample and the Wuliangsuhai No. 2 ice sample. Arctic sea ice samples were collected from field stations during China's ninth scientific expedition, located at 79°13′ N, 168°49′ W and 84°24′ N, 156°08′ E, respectively. The growth of sea ice is influenced by seawater salinity, which leads to widely distributed brine bubbles and channels. Two ice samples were collected in the Arctic, named the Arctic No. 1 ice sample and the Arctic No. 2 ice sample. Field-collected ice samples were placed in ice core bags, which were stored in a cooler covered with crushed ice and snow (temperature −5 °C). A total of 2987 ice CT images were obtained by scanning the ice samples layer by layer, which were used to statistically analyze threshold range of multiphase components of natural ice. The flow of experimental processing is shown in Figure 1.
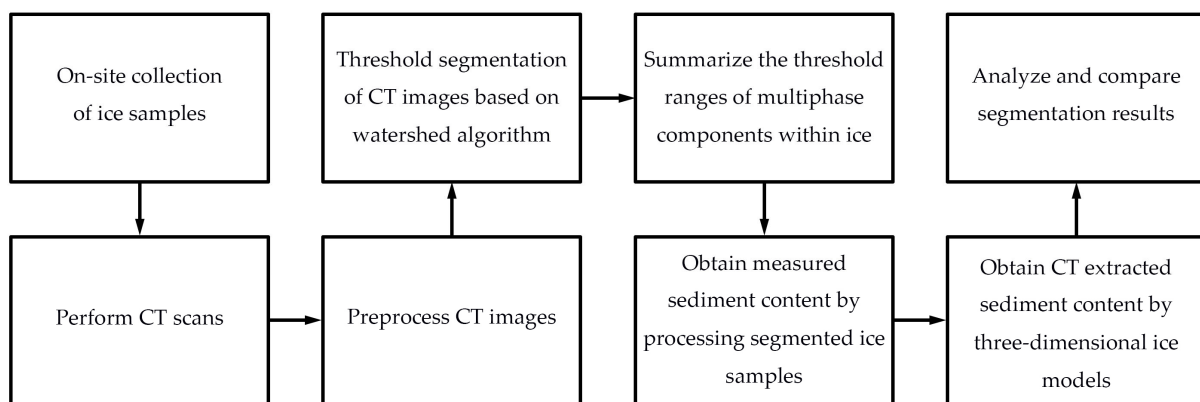

Figure 1. Flow chart of the experimental processing.

2.2. Experimental Equipment and Scanning Principle

The CT scanning test was performed by a Philips Brilliance 16 CT scanning experimental machine in Cold and Arid Regions Environmental and Engineering Research Institute, Chinese Academy of Sciences, Lanzhou. The instrument's main technical parameters are shown in Table 1.

Table 1. Main technical parameters of CT instrument.

	Scan Cross Section (mm^2)	Scan Layer Thickness (mm)	Scan Voltage (kV)	Scan Current (mA)	Reconstruction Matrix
Technical parameters	200×200	3	120	313	1024×1024

The CT scan system typically comprises an X-ray source, a sample platform, a detector, and a computer system for data analysis. As X-ray penetrates the sample, the X-ray energy decreases due to photoelectric absorption, Compton effect, and electron pair effect [24]. The intensity decay law of X-ray is shown in Equation (1) [25]:

$$I = I_0 \exp[-\mu x] \tag{1}$$

where I is the X-ray transmission intensity, I_0 is the X-ray incident intensity, μ is the linear attenuation coefficient of the material, x is the path length of the X-rays through the material.

The CT system operates by determining the attenuation coefficient of X-rays within the scanned object, and the attenuation coefficient distribution matrix on the scanning cross section is established by computer system. In practical applications, the differences in attenuation coefficients between materials are minimal, so the CT values (Hounsfield unit, Hu) are introduced to amplify this difference, and the CT value of water is set to 0 Hu [26], as shown in Equation (2):

$$CT_{number} = \frac{\mu - \mu_w}{\mu_w} \times 1000 \tag{2}$$

where CT_{number} is the CT value, μ_w is the attenuation coefficient of water.

The CT value increases with the material's density, which can provide information about the density of the scanning section. In the experiment, seven samples of the Yellow River ice, two samples of Wuliangsuhai lake ice and two samples of Arctic sea ice were scanned by CT, yielding microstructural images of these three different types of ice. The scanning section was parallel to the ice core profile, then, the ice samples were scanned layer by layer along the depth direction with a scanning section of 200 mm × 200 mm, a layer spacing of 3 mm, and a CT image reconstruction matrix size of 1024 × 1024 pixels.

2.3. CT Image Preprocessing

During the acquisition of CT images, inherent electronic device perturbations and environmental influences result in the production of noise and distortion, which negatively impact the segmentation and extraction of components [27]. To mitigate image noise, the Median filtering algorithm was employed. Additionally, manual cutting of the ice samples resulted in surface imperfections, such as breakages and protrusions. Moreover, the outer air portion of the CT image was not the test subject. To eliminate the potential interference from these parts, the images were cropped, as shown in Figure 2, with the research area highlighted in the red frame.
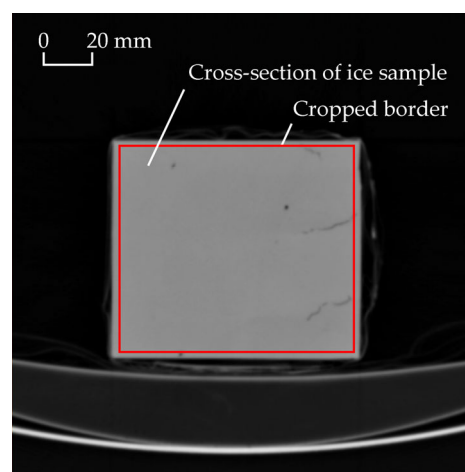

Figure 2. CT original image and research area frame.

2.4. Watershed Algorithm

Natural ice contains a significant number of impurities that vary in composition, leading to complex and heterogeneous structures. The CT value denotes the attenuation coefficient of X-rays reaching the detection point, which is related to the density of each component within the ice sample. The range of machine detection is from −1024 Hu to 3071 Hu. However, the CT values displayed in the images correspond only to a grayscale range of 0 to 255. As shown in Figure 3, the CT value ranges of gas, ice, unfrozen water, and sediment within the samples are similar without significant intervals. This proximity leads to uncertainty in artificially determining the segmentation thresholds and unsuitability of the global threshold segmentation methods. The boundary between the multiphase components within ice is indistinct. To extract the distribution, morphology, and spatial location of the multiphase components within ice, the generation of closed region boundaries is necessary.
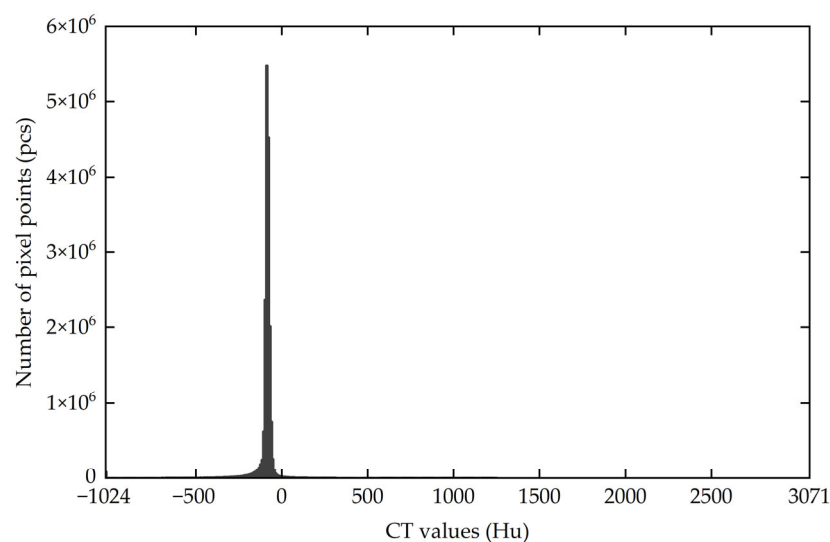
Figure 3. Histogram of ice sample CT values. There are no peaks and valleys in the CT value histograms, which proves that the CT values range of gas, unfrozen water, ice, and sediment within the samples are similar without significant intervals.

The watershed algorithm simulates the process of water immersion, which is suitable for processing multiple objects and complex edge structures in images to form closed boundaries. The algorithm treats the image as a topographical surface, with the gray value of each pixel representing the terrain elevation [28]. Local minima in the image serve as the points from which water continuously immerses, and the water gradually floods the corresponding basin of image. As the water levels in two different regions rise and converge, a dam is formed at their junction. Upon completion of the overflow process, each local minimum is encircled by the dam corresponding to its water accumulation basin, and each dam serves as the watershed. Consequently, the boundary of multiphase components within ice is clearly extracted [29], as shown in Figure 4. Different water accumulation basins represent different partitions of the image, thereby achieving image segmentation.

The CT values of gas, ice and unfrozen water are all less than or equal to zero. In contrast, high CT values in freshwater ice are indicative of sediment, while high CT values in sea ice are indicative of brine. The ice sample is considered to be composed of gas, ice, water, and sediment (brine). The CT value ranges of gas, ice, water, and sediment (brine) within the ice samples are determined by combining with the watershed algorithm, which offers a novel technical method for the segmentation of ice CT images.
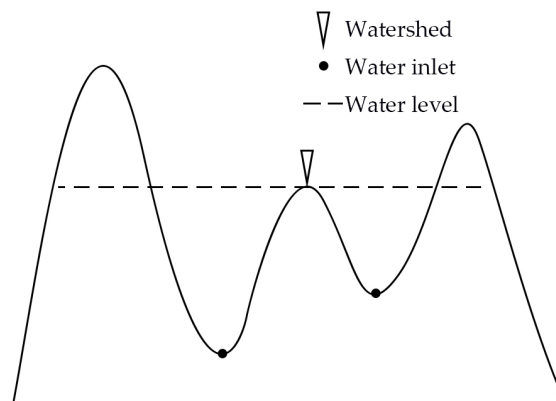
Figure 4. Schematic diagram of watershed algorithm model.

The watershed algorithm first defines the two-dimensional image I as a grayscale image set to discrete values of $[0, N]$, where N is the positive integer, D is the set of positive integers, and p is the pixel of the image. The set of pixels T_h with height less than h is filtered in the two-dimensional image I, where h is the threshold value [30], as shown in Equation (3).

$$T_h = \{p \in D \,|\, I(p) \leq h\} \tag{3}$$

For the set A and B, d_A (a, b) denotes the shortest distance between two points a, b in the set A. If $B \subseteq A$ is satisfied, then B is randomly divided into k mutually interconnected parts, which is denoted as B_i ($i = 1, 2, \ldots, k$), and B_i corresponds to the geodesic influence zone solution formula is defined as Equation (4) [30].

$$iz_A(B_i) = \{p \in A \,|\, d_A(p, B) < d_A(p, B/B_i)\} \tag{4}$$

The set $IZ_A(B)$ is the union of B's geodetic influence zone defined as Equation (5) [30].

$$IZ_A(B) = \overset{k}{\underset{i=1}{\cup}} iz_A(B_i) \tag{5}$$

In A, the complementary set of $IZ_A(B)$ is called $SKIZ_A(B)$ (Skeleton of Geodetic Influence Zone) as in Equation (6) [30].

$$SKIZ_A(B) = A/IZ_A(B) \tag{6}$$

The pixels in the foreground area are aggregated to obtain the $SKIZ$, as shown in iterative Equation (7) [30].

$$\begin{cases} X_{h_{\min}} = \{p \in D \,|\, I(p) \leq h_{\min}\} = T_{h_{\min}} \\ X_{h+1} = MIN_{h+1} \cup IZ_{h+1}(X_h), h \in [h_{\min}, h_{\max}] \end{cases} \tag{7}$$

where h is the range of gray value, X_{hmin} is the pixel point with the smallest gray value in image I, h_{min} is the smallest gray value, h_{max} is the largest gray value, T_{hmin} is the set of pixels with minimum value points in each basin, X_{h+1} is all pixels with gray value less than $h + 1$, MIN_{h+1} is the set of pixel points with minimum gray value regenerated at the $h + 1$, $IZ_{h+1}(X_h)$ denotes the set of individual regions divided on the basis of the shortest distance within all T_{h+1} connected regions.

In D, the complementary set of X_{hmin} is watershed region X_{Wshed}, as shown in Equation (8) [30].

$$X_{Wshed} = D/X_{h_{\min}} \tag{8}$$

2.5. Sediment Content

Due to the proximity of the CT value ranges of gas, ice, unfrozen water and sediment within the samples, which makes it impossible to validate the accuracy of segmentation results through subjective awareness. Furthermore, there is no precise and effective method to obtain the content of each component in the ice samples except sediment. In order to quantitatively validate the accuracy of the segmentation results, this study measured the sediment content per unit volume of ice sample by melting a certain volume of the Yellow River ice samples into a bottle, followed by filtering, drying, and weighing the sediment in the ice sample, as shown in Equation (9).

$$S_m = m/V_i \tag{9}$$

where S_m is the measured sediment content, m is the dried sediment mass in the ice sample, V_i is the volume of corresponding ice sample.

Moreover, the sediment content was extracted from the reconstructed three-dimensional model. This study compared the error between the measured sediment content and the CT extracted sediment content, as shown in Equation (10).

$$S_{CT} = (\rho_s \times V_s)/V_i \tag{10}$$

where S_{CT} is the sediment content extracted from the CT three-dimensional model, ρ_s is the density of dried sand, V_s is the volume of sediment extracted from the CT three-dimensional model.

3. Results

3.1. Threshold Range and Two-Dimensional Image Segmentation Results

According to the multi-threshold segmentation results, the CT values of various components within the ice were statistically summarized. The lower limit of gas CT values fluctuated widely. For example, the Yellow River No.2 ice sample was dominated by trapped bubbles (The CT values of No.2 ice sample's gas ranged from −212 Hu~−107 Hu). Bubbles were small and hermetic, which contained high water vapor. Strip shaped pores were present in the Yellow River No.3 ice sample (The CT values of No.3 ice sample's gas ranged from −269 Hu~−115 Hu), but the pore structure was elongated and hermetic, restricting air circulation. However, open and flaky cracks were present in the ice samples of the Yellow River No. 1, 4, 5, 6 and 7, resulting in the lower limit values being close to air's CT value (−1000 Hu). To ensure the universal applicability of the CT value ranges, the minimum and maximum values of various components in multiple ice samples were, respectively, used as the lower and upper limits for CT values, as shown in Table 2. The CT values of gas ranged from −1024 Hu~−107 Hu. The CT values of ice ranged from −103 Hu to −50 Hu. The CT values of unfrozen water ranged from −8 Hu to 18 Hu. Due to the differing mineral compositions in the sediment, the upper limit of sediment CT values fluctuated widely, and this value did not have an effect on the image segmentation. In this paper, the CT maximum value of the instrument's technical parameters was taken as the upper limit value of sediment, the CT values of sediment ranged from 20 Hu~3071 Hu.

Table 2. Statistical results of various components' CT values in the Yellow River ice.

	The Yellow River Ice	
	Lower Limit Value (Hu)	**Upper Limit Value (Hu)**
gas	-	−107
ice	−103	−50
unfrozen water	−8	18
sediment	20	-

In the case of the Yellow River ice, the field sample exhibited a white and transparent appearance, as shown in Figure 5a. The sediment content was particularly high in the middle portion of the ice sample (17 cm~30 cm from the bottom of the ice sample), with a greater number of spherical bubbles in the upper portion of the sediment layer. Deng et al. found that the bubbles in the Yellow River ice during the freezing period were mainly spherical using the Federov rotary stage. Moreover, there is no significant correlation between the equivalent diameter of bubbles in ice and depth [31]. The CT image was segmented into four regions based on the CT value ranges, where gray represented gas, dark blue represented unfrozen water, orange represented sediment, and light blue represented ice, as shown in Figure 5b–j. Figure 5h showed the top of the ice sample, which exhibited an abundance of gasses and lacked both sediment and unfrozen water. Figure 5i showed the layer at 25 cm from the bottom of ice sample, containing sediment, unfrozen water, gas, and ice. The sediment within the ice sample was randomly distributed on the plane, with some sediment adhering to the edges of irregularly shaped bubbles. Unfrozen water occurred with the sediment as well as in small, isolated bubbles. The shapes of bubbles were predominantly single spheres or combinations of multiple spheres. Figure 5j showed the bottom of the ice sample, which contained a little sediment and unfrozen water. It matched the visual observation of samples collected in the field.
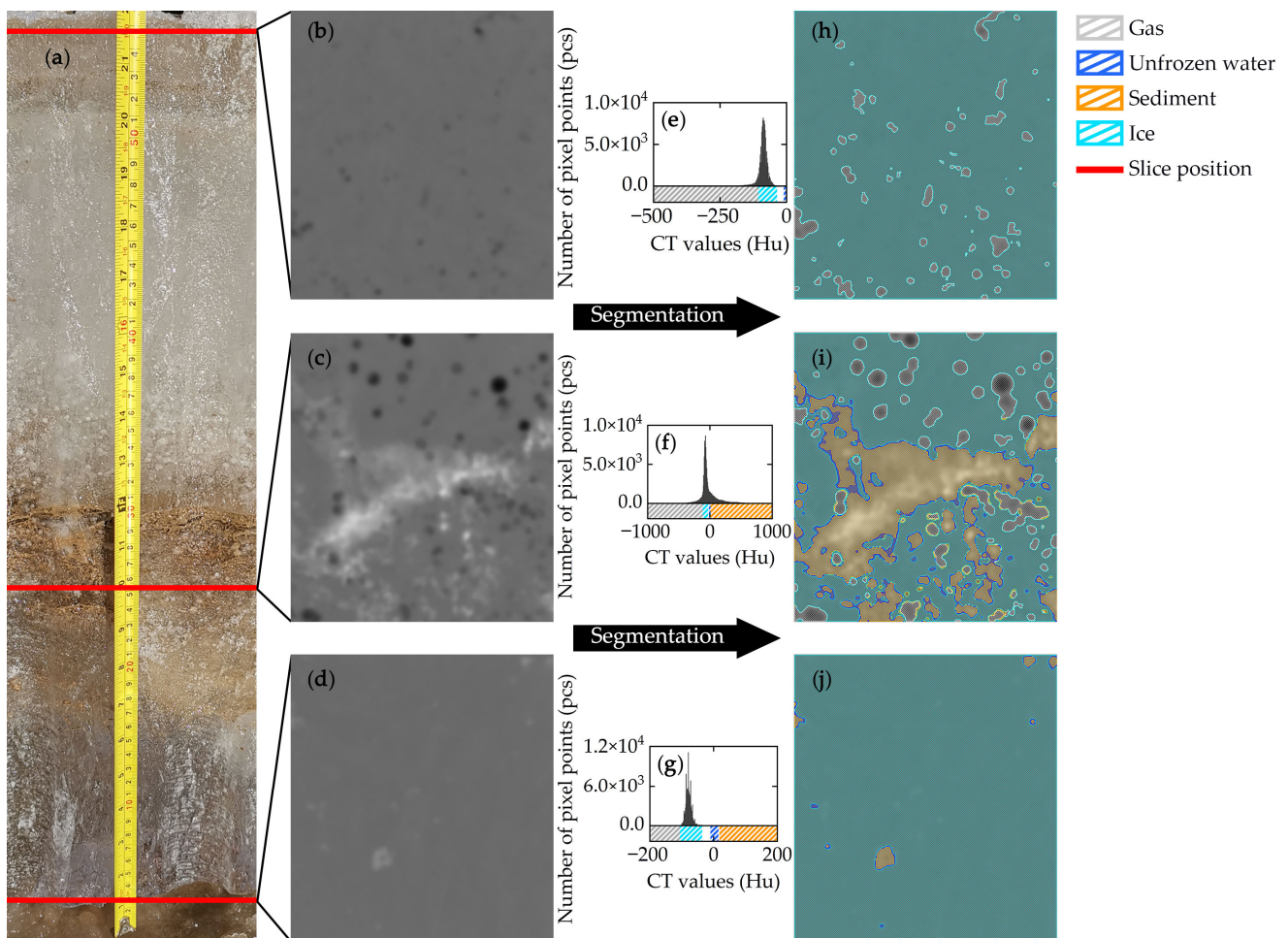

Figure 5. Schematic of sample collection and two-dimensional image threshold segmentation. (**a**) The Yellow River ice sample. Original two-dimensional CT images of (**b**) top layer, (**c**) 25 cm from the bottom layer, (**d**) bottom layer. Histograms of CT values for (**e**) top layer, (**f**) 25 cm from the bottom layer, (**g**) bottom layer. Two-dimensional image multi-threshold segmentation results of (**h**) top layer, (**i**) 25 cm from the bottom layer, (**j**) bottom layer.

The bubbles in the Wuliangsuhai lake ice were small and sealed, as shown in Table 3. The CT values of Wuliangsuhai No. 1 ice sample's gas ranged from −186 Hu~−103 Hu, which were comparable to the CT values of the Yellow River No. 2 ice sample's gas (−212 Hu~−107 Hu). Notably, the CT lower limit value of Wuliangsuhai lake ice's gas was slightly larger than that of the Yellow River ice's gas. It could be inferred that the bubbles in the Wuliangsuhai lake ice may contain higher concentrations of gasses, such as oxygen and carbon dioxide produced by biological communities, as well as water vapor. Consequently, the density inside the Wuliangsuhai lake ice's bubbles was slightly higher than the density inside the Yellow River ice's bubbles. The CT values of Wuliangsuhai lake ice's gas ranged from −1024 Hu~−103 Hu. The CT values of Wuliangsuhai lake ice ranged from −100 Hu~−38 Hu. The lower limit was close to that of the Yellow River ice, while the upper limit was slightly higher. This difference can be attributed to the reduced hydrodynamic influence during the freezing process in Wuliangsuhai lake, leading to a more compact and stable ice structure. The CT values of unfrozen water ranged from −8 Hu~13 Hu. Additionally, the stable hydrodynamic environment also contributed to low sediment content in the Wuliangsuhai lake ice, with only tiny amounts of sediment found in the Wuliangsuhai No. 1 ice sample.

Table 3. Statistical results of various components' CT values in the Wuliangsuhai lake ice.

	Wuliangsuhai Lake Ice	
	Lower Limit Value (Hu)	Upper Limit Value (Hu)
Gas	-	−103
Ice	−100	−38
Unfrozen Water	−8	13
Sediment	20	-

The pore structures in the Arctic sea ice were dominated by strip-shaped brine channels, egg-shaped trapped bubbles, and irregular-shaped extruded bubbles, which were large and interconnected. The CT lower limit value of gas in sea ice was close to that of air, indicating that the pores were connected to the outside. As shown in Table 4, the CT values of gas ranged from −1024 Hu~−160 Hu. The CT values of Arctic sea ice ranged from −153 Hu~−51 Hu. Ji et al. reviewed sea ice density measurement data during 2000–2015 and found Arctic sea ice density ranged from 675 kg/m^3 to 954 kg/m^3 [32]. Zhang et al. measured the densities of the Yellow River ice and Wuliangsuhai lake ice during 2017–2020. The Yellow River ice density ranged from 703 kg/m^3 to 965 kg/m^3 and Wuliangsuhai lake ice density ranged from 883 kg/m^3 to 907 kg/m^3 [2]. Since the density of sea ice was lower than the density of freshwater ice, the CT lower limit value of Arctic sea ice was also lower than that of the Yellow River ice and the Wuliangsuhai lake ice. The CT values of brine ranged from −6 Hu~3071 Hu, with the upper limit being determined by salinity, which increases with increasing salinity.

Table 4. Statistical results of various components' CT values in the Arctic sea ice.

	Arctic Sea Ice	
	Lower Limit Value (Hu)	Upper Limit Value (Hu)
Gas	-	−160
Ice	−153	−51
Brine	−6	-

3.2. Three-Dimensional Reconstructed Images of Ice

Common bubbles in ice can be categorized into three types: trapped bubbles, closed bubbles, and extruded bubbles. These bubbles differ significantly in their formation processes and physical properties [33]. Trapped bubbles form due to the lower solubility of air in ice compared to its solubility in water. During the freezing process, air is expelled

from the ice to the freezing front. When the gas concentration at the freezing front reaches a supersaturation level, bubble nucleation occurs. As the freezing front moves, the high gas concentration surrounding the bubble diffuses into it, facilitating its growth. If the gas escape rate is slower than the freezing rate, the freezing front gradually covers the air bubbles, ultimately resulting in the formation of trapped bubbles, which typically exhibit egg-like or needle-like shapes. Closed bubbles are commonly found in high-latitude alpine lakes, and the formation process involves the freezing of methane and other gasses produced by microbial fermentation on the lakebed, resulting in primarily disk-shaped bubbles. Extruded bubbles are found in the deep ice cores of polar ice sheets. The formation process involves the gradual transformation of fluffy polar snow into ice through gravitational extrusion, resulting in the entrapment of irregularly shaped bubbles within the ice. Two-dimensional CT images can only provide localized information. To comprehensively represent the segmentation effect of ice samples, a three-dimensional model of the ice is reconstructed intuitively and stereoscopically by stacking multiple layers of two-dimensional images. According to model data, the surface of the Yellow River ice had begun to melt and formed vertical ice, which was dominated by strip-shaped pores, as shown in Figure 6a,b, and trapped bubbles, as shown in Figure 6c,d. The high sediment content (20 to 400 g/L) of the Yellow River significantly impacted the generation and elimination process of river ice, with sediment randomly frozen within the ice [34], as shown in Figure 6c.
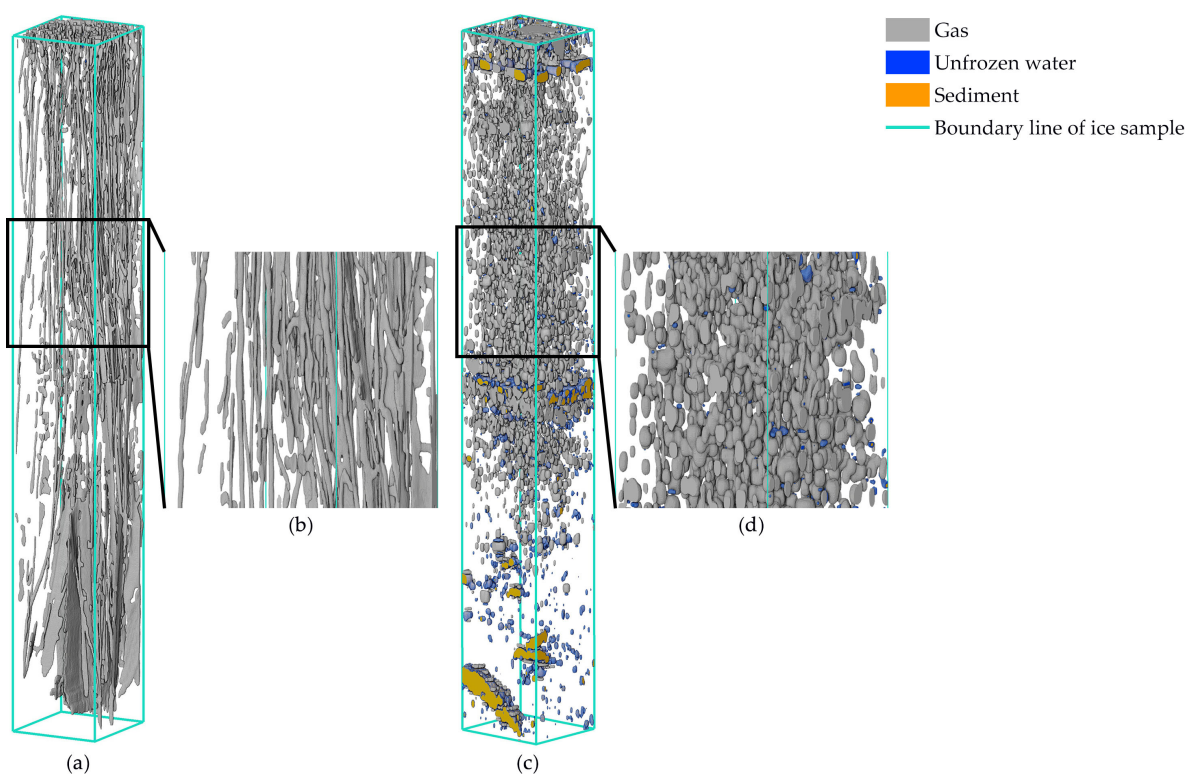

Figure 6. Three-dimensional reconstructed images of the Yellow River ice samples. Global three-dimensional image of (**a**) the Yellow River No. 3 ice sample, and (**c**) the Yellow River No. 4 ice sample. Local three-dimensional images of (**b**) the Yellow River No. 3 ice sample, and (**d**) the Yellow River No. 4 ice sample.

In contrast to the complex hydrodynamic conditions of the Yellow River, the Wuliangsuhai lake ice experienced stable hydrodynamic conditions during its freezing process. As a result, the lake ice had a complete structure, devoid of open cracks or flaky bubbles, whose porosity was significantly lower than that of the Yellow River. The collection zone of the Wuliangsuhai No. 1 ice sample appeared white with distinct boundary lines, as shown in Figure 7a. The air bubbles within the Wuliangsuhai No. 1 ice sample were predominantly

closed bubbles, which were disk-shaped and in bunches, as shown in Figure 7b,c. These closed bubbles formed when gasses produced by aquatic organisms' respiration could not be discharged in time and were frozen within the ice, suggesting the presence of substantial, stable plant or microbial communities beneath the area where the Wuliangsuhai No. 1 ice sample was collected. Zhang et al. simulated and analyzed changes in dissolved oxygen during growth and stability period of ice. The Wuliangsuhai's maximum daily average oxygen production rate was 7.19 mg/(L·d) [35]. The low porosity and small-volume bubbles of Wuliangsuhai No. 2 ice sample, as shown in Figure 7d,e, proved that Wuliangsuhai No. 2 ice sample was less affected by the external environment during the process of generation.
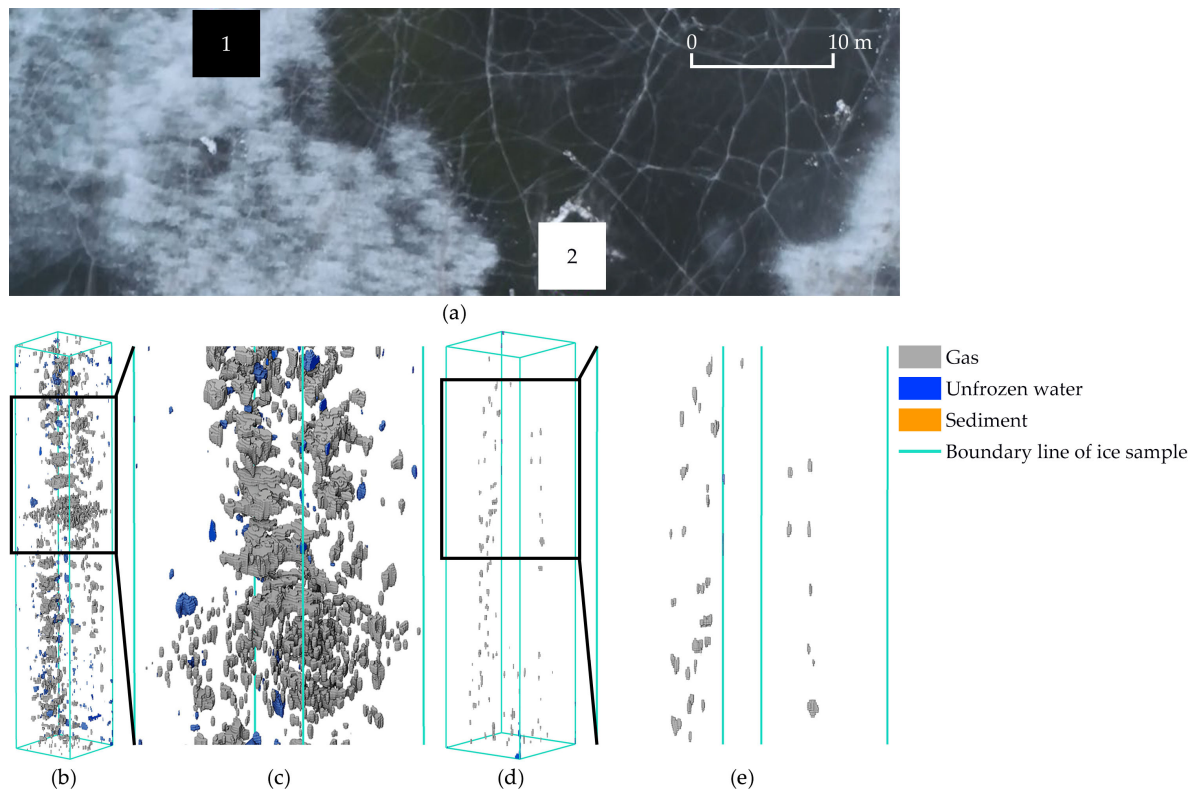

Figure 7. Study area and local three-dimensional reconstructed images of the Wuliangsuhai lake ice. (**a**) the Wuliangsuhai No. 1 and No. 2 ice samples collection areas. Global three-dimensional images of (**b**) the Wuliangsuhai No. 1 ice sample, and (**d**) the Wuliangsuhai No. 2 ice sample. Local three-dimensional images of (**c**) the Wuliangsuhai No. 1 ice sample, and (**e**) the Wuliangsuhai No. 2 ice sample.

In contrast to the Yellow River ice and Wuliangsuhai lake ice, Arctic sea ice was not affected by sediment during its generation and elimination process, but rather by seawater salinity. Although, more than 80% of the salt was expelled during freezing, but salt still remained in the form of brine cells within the sea ice. Under constant low-temperature conditions (0 °C~−30 °C), the high concentration brine within the sea ice always remained in the liquid state. Due to the higher specific gravity of brine compared to that of ice crystals, it was influenced by gravity to move down along the ice crystal gaps, resulting in the formation of brine channels. As shown in Figure 8a,b, the spherical or strip-shaped brine cells were mainly attached to the pore structures, while the pores were mainly downward strip-shaped brine channels.
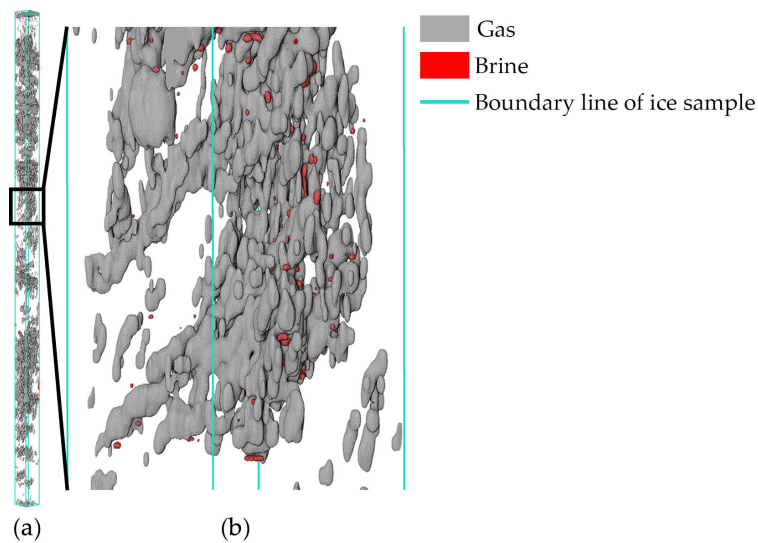
Figure 8. Global three-dimensional image of (**a**) the Arctic No. 1 ice sample. Local three-dimensional image of (**b**) the Arctic No. 1 ice sample.

3.3. Comparison of CT Extracted Sediment Content with Measured Sediment Content

The CT value range is -1024 Hu~3071 Hu, which corresponds to 0~255 levels of gray value on the CT image, with each gray level representing 16 Hu. Furthermore, the proximity of the CT value ranges of gas, ice, and unfrozen water within the samples, as well as the large amount of image data, makes it impossible to validate the accuracy of segmentation results through subjective awareness. In order to quantitatively validate the accuracy of the segmentation results, this study measured the sediment content per unit volume of ice sample by melting a certain volume of the Yellow River ice samples into a bottle, followed by filtering, drying, and weighing the ice sample. Meanwhile, the volume of sediment within the ice sample was obtained based on the CT three-dimensional model. The dry density of sediment was set to 1.4 g/cm^3 to calculate the sediment content in the CT data [36], as shown in Figure 9. The errors between the measured data and the CT extracted data were less than 0.003 g/cm^3. The results showed that the ice three-dimensional model based on the watershed algorithm aligned well with the measured data, demonstrating consistent trends in both sets of results.
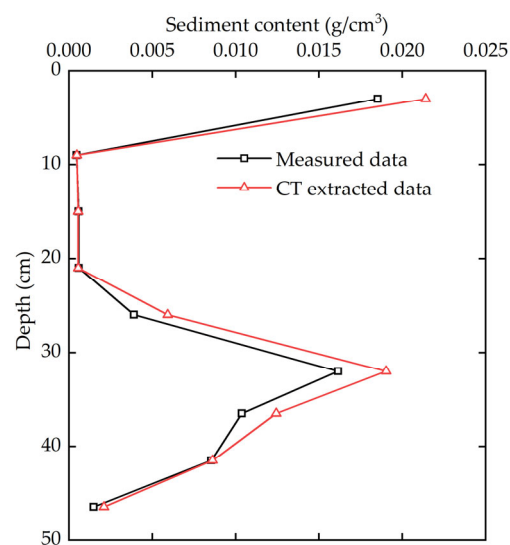

Figure 9. Distribution of sediment content in the Yellow River ice along the depth direction.

4. Conclusions

Ice multiphase components not only reflected the ice growth process, but also significantly influenced the mechanical, thermal, optical, and electrical properties of ice. However, the CT value ranges of gas, ice, unfrozen water, and sediment were close to each other, making it challenging to determine segmentation thresholds artificially. This study determined the threshold ranges for multiphase components of the Yellow River ice, Wuliangsuhai lake ice and Arctic sea ice based on X-ray computed tomography and watershed algorithm, which provided a reference for the threshold ranges of ice experiments. The main conclusions were as follows.

1. X-ray computed tomography combined with the watershed algorithm was an efficient and reliable method for obtaining internal microstructural information of ice without destruction. This approach could determine the multi-threshold value of CT image to segment the ice samples into various components, such as gas, ice, unfrozen water, and sediment (brine). According to the multi-threshold segmentation results, the three-dimensional ice model was constructed to obtain the morphology and spatial distribution of various components within the ice samples, which provided a scientific basis for ice engineering, ice remote sensing, and ice disaster prevention.
2. The gas CT values of the Yellow River ice, the Wuliangsuhai lake ice, and the Arctic sea ice ranged from -1024 Hu~-107 Hu, -1024 Hu~-103 Hu, -1024 Hu~-160 Hu, respectively. The Yellow River ice and the Wuliangsuhai lake ice were dominated by egg-shaped trapped bubbles and disk-shaped closed bubbles. The Arctic sea ice was dominated by strip-shaped brine channels and irregular-shaped extruded bubbles. The ice CT values of the Yellow River ice, the Wuliangsuhai lake ice and the Arctic sea ice ranged from -103 Hu~-50 Hu, -100 Hu~-38 Hu, -153 Hu~-51 Hu. In contrast to the Yellow River ice and the Arctic sea ice, the Wuliangsuhai lake ice had a more compact structure. The unfrozen water CT values of the Yellow River ice and the Wuliangsuhai lake ice ranged from -8 Hu~18 Hu, -8 Hu~13 Hu. The sediment CT values of the Yellow River ice and the Wuliangsuhai lake ice ranged from 20 Hu~3071 Hu, 20 Hu~3071 Hu, and the brine CT values of the Arctic sea ice ranged from -6 Hu~3071 Hu.
3. High sediment content of the Yellow River significantly impacted the generation and elimination process of river ice, with sediment randomly frozen within the ice. At the same time, the sediment was surrounded by a lot of unfrozen water, which was significantly higher than the unfrozen water content in the sediment-free zone.
4. The three-dimensional ice model based on X-ray computed tomography and watershed algorithm was in good agreement with the measured data, exhibiting errors of less than 0.003 g/cm^3. It could provide a new idea for quantitative study of ice microstructure information. This study only verified the accuracy of sediment content. In further research, we need to use nuclear magnetic resonance instruments to verify the accuracy of gas and liquid phases in ice samples.

Author Contributions: Conceptualization, Z.L.; methodology, S.H. and Z.L.; investigation, S.H. and Q.W.; data curation, S.H., C.L. and Z.L.; writing—original draft preparation, S.H.; writing—review and editing, S.H., Q.W. and C.L.; project administration, Q.W. and Z.L.; funding acquisition, Q.W. and Z.L. All authors have read and agreed to the published version of the manuscript.

Data Availability Statement: The data are available in the case that it is required.

References

1. Müller-Stoffels, M.; Langhorne, P.J.; Petrich, C.; Kempema, E.W. Preferred crystal orientation in fresh water ice. *Cold Reg. Sci. Technol.* **2009**, *56*, 1–9. [CrossRef]
2. Zhang, Y.D.; Li, Z.J.; Li, C.J.; Zhang, B.S.; Deng, Y. Microstructure characteristics of river ice in Inner Mongolia section of the Yellow River and its influencing factors. *J. Hydraulic Eng.* **2021**, *52*, 1418–1429. [CrossRef]
3. Timco, G.; Weeks, W. A review of the engineering properties of sea ice. *Cold Reg. Sci. Technol.* **2010**, *60*, 107–129. [CrossRef]
4. Huang, W.F.; Han, H.W.; Shi, L.Q.; Niu, F.J.; Deng, Y.S.; Li, Z.J. Effective thermal conductivity of thermokarst lake ice in Beiluhe Basin, Qinghai-Tibet Plateau. *Cold Reg. Sci. Technol.* **2013**, *85*, 34–41. [CrossRef]
5. Rødtang, E.; John, J.; Alfredsen, K.; Høyland, K. In-situ ice strength distribution of anchor ice dams. *Cold Reg. Sci. Technol.* **2023**, *215*, 103982. [CrossRef]
6. Deng, Y.; Li, Z.K.; Wang, J.; Xu, L.K. The microstructure of Yellow River ice in the freezing period. *Crystals* **2019**, *9*, 484. [CrossRef]
7. Misra, R.; Chung, T.F.; Lin, S.C. Understanding microstructural evolution during three–axial thermos–mechanical processing involving severe plastic deformation of magnesium alloys. *Mater. Technol.* **2024**, *39*, 2350220. [CrossRef]
8. Mel'nichenko, N.; Tyveev, A.; Lazaryuk, A.Y.; Savchenko, V.; Kustova, E. Vertical distribution of brine and volume structure of thin annual ice in Amursky Bay based on the methods of nuclear magnetic resonance and magnetic resonance imaging. *Oceanology* **2019**, *59*, 777–786. [CrossRef]
9. Kawamura, T. Observations of the internal structure of sea ice by X-ray computed tomography. *J. Geophys. Res. Ocean.* **1988**, *93*, 2343–2350. [CrossRef]
10. Michel, B.; Ramseier, R.O. Classification of river and lake ice. *Can. Geotech. J.* **1971**, *8*, 36–45. [CrossRef]
11. Shokr, M.E.; Sinha, N.K. Arctic Sea ice microstructure observations relevant to microwave scattering. *Arctic* **1994**, *47*, 265–279. [CrossRef]
12. Cole, D.M. The microstructure of ice and its influence on mechanical properties. *Eng. Fract. Mech.* **2001**, *68*, 1797–1822. [CrossRef]
13. Li, Z.J.; Zhang, L.M.; Lu, P.; Leppäranta, M.; Li, G.W. Experimental study on the effect of porosity on the uniaxial compressive strength of sea ice in Bohai Sea. *Sci. China Technol. Sci.* **2011**, *54*, 2429–2436. [CrossRef]
14. Sammonds, P.; Montagnat, M.; Bons, P.; Schneebeli, M. Ice microstructures and microdynamics. *Phil. Trans. R. Soc. A.* **2017**, *375*, 20160438. [CrossRef] [PubMed]
15. Hammonds, K.; Baker, I. Quantifying damage in polycrystalline ice via X-ray computed micro-tomography. *Acta Mater.* **2017**, *127*, 463–470. [CrossRef]
16. Salomon, M.L.; Maus, S.; Petrich, C. Microstructure evolution of young sea ice from a Svalbard fjord using micro-CT analysis. *J. Glaciol.* **2022**, *68*, 571–590. [CrossRef]
17. Du Plessis, A.; Le Roux, S.G.; Guelpa, A. Comparison of medical and industrial X-ray computed tomography for non-destructive testing. *Case Stud. Nondestruct. Test. Eval.* **2016**, *6*, 17–25. [CrossRef]
18. Zeng, Q.; Chen, S.; Yang, P.C.; Peng, Y.; Wang, J.Y.; Zhou, C.S.; Wang, Z.D.; Yan, D.M. Reassessment of mercury intrusion porosimetry for characterizing the pore structure of cement-based porous materials by monitoring the mercury entrapments with X-ray computed tomography. *Cem. Concr. Compos.* **2020**, *113*, 103726. [CrossRef]
19. Wang, H.N.; Ni, W.K. Quantitative analysis of loess microstructure based on CT and SEM images. *Rock Soil Mech.* **2012**, *33*, 243–247. (In Chinese) [CrossRef]
20. Zhang, X.N.; Wan, C.; Wang, D.; He, L.F. Numerical simulation of asphalt mixture based on three-dimensional heterogeneous specimen. *J. Cent. South Univ. Technol.* **2011**, *18*, 2201–2206. [CrossRef]
21. Ge, Z.D.; Chen, L.X.; Luo, R.; Wang, Y.W.; Zhou, Y.C. The detection of structure in wood by X-ray CT imaging technique. *BioResources* **2018**, *13*, 3674–3685. [CrossRef]
22. Zhang, Z.B.; Zou, Y.N.; Huang, Y.L.; Li, Q. CT image crack segmentation method based on linear feature enhancement. *J. X-Ray Sci. Technol.* **2022**, *30*, 903–917. [CrossRef] [PubMed]
23. Cui, Z.M.; Zhao, S.N.; Shi, X.H.; Lu, J.P.; Liu, Y.; Liu, Y.H.; Zhao, Y.X. Vertical distribution characteristics and ecological risk assessment of mercury and arsenic in ice, water, and sediment at a cold-arid lake. *Toxics* **2024**, *12*, 540. [CrossRef]
24. Ketcham, R.A.; Carlson, W.D. Acquisition, optimization and interpretation of X-ray computed tomographic imagery: Applications to the geosciences. *Comput. Geosci.* **2001**, *27*, 381–400. [CrossRef]
25. Zhang, S.J.; Lai, Y.M.; Zhang, X.F.; Pu, Y.B.; Yu, W.B. Study on the damage propagation of surrounding rock from a cold-region tunnel under freeze–thaw cycle condition. *Tunn. Undergr. Space Technol.* **2004**, *19*, 295–302. [CrossRef]
26. Rabba, J.A.; Jaafar, H.A.; Suhaimi, F.M.; Jafri, M.Z.M.; Osman, N.D. A simplified low-cost phantom for image quality assessment of dental cone beam computed tomography unit. *J. Med. Radiat. Sci.* **2024**, *71*, 78–84. [CrossRef]
27. Jing, D.J.; Meng, X.X.; Ge, S.C.; Zhang, T.; Ma, M.X.; Tong, L.Q. Reconstruction and seepage simulation of a coal pore–fracture network based on CT technology. *PLoS ONE* **2021**, *16*, e0252277. [CrossRef]
28. Rambabu, C.; Chakrabarti, I. An efficient immersion-based watershed transform method and its prototype architecture. *J. Syst. Architect.* **2007**, *53*, 210–226. [CrossRef]
29. Qin, Y.B.; Wang, W.; Liu, W.; Yuan, N. Extended-maxima transform watershed segmentation algorithm for touching corn kernels. *Adv. Mech. Eng.* **2013**, *5*, 268046. [CrossRef]
30. Shen, X.J.; Wu, X.Y.; Han, D.J. Survey of research on watershed segmentation algorithms. *Comput. Eng.* **2015**, *41*, 26–30. (In Chinese) [CrossRef]

31.   Deng, Y.; Wang, J.; Zhou, J.; Zhang, P. Quantitative analysis of the geometrically representative volume element of the Yellow River's granular ice microstructure during the freezing period. *Crystals* **2023**, *13*, 1021. [CrossRef]

32.   Ji, Q.; Li, B.J.; Pang, X.P.; Zhao, X.; Lei, R.B. Arctic Sea ice density observation and its impact on sea ice thickness retrieval from CryoSat–2. *Cold Reg. Sci. Technol.* **2021**, *181*, 103177. [CrossRef]

33.   Yoshimura, K.; Inada, T.; Koyama, S. Growth of spherical and cylindrical oxygen bubbles at an ice-water interface. *Cryst. Growth Des.* **2008**, *8*, 2108–2115. [CrossRef]

34.   Ni, J.R.; Sun, L.Y.; Sun, W.L. Modification of chemical oxygen demand monitoring in the Yellow River, China, with a high content of sediments. *Water Environ. Res.* **2007**, *79*, 2336–2342. [CrossRef]

35.   Zhang, F.; Shi, X.H.; Zhao, S.N.; Hao, R.N.; Zhai, J.L. Equilibrium analysis of dissolved oxygen in Lake Wuliangsuhai during ice-covered period. *J. Lake Sci.* **2022**, *34*, 1570–1583. (In Chinese) [CrossRef]

36.   Qi, P.; Ji, M.X.; Sun, Z.Y. Formation mechanism of hyper-concentrated sediment flow caused by scouring of reservoir emptying. *J. Hydraul. Eng.* **2006**, *8*, 906–912. (In Chinese) [CrossRef]